Evaluation of the γn→π^{−}p differential cross section in the Δ-isobar region

W. J. Briscoe, A. E. Kudryavtsev, P. Pedroni, I. I. Strakovsky, V. E. Tarasov, and R. L. Workman

Phys. Rev. C **86**, 065207 — Published 20 December 2012

DOI: 10.1103/PhysRevC.86.065207

Evaluation of the $\gamma n \to \pi^- p$ differential cross section in the Δ-isobar region

W. J. Briscoe[1], A. E. Kudryavtsev[2,1], P. Pedroni[3], I. I. Strakovsky[1], V. E. Tarasov[2], R. L. Workman[1]

[1] *The George Washington University, Washington, DC 20052, USA*
[2] *Institute of Theoretical and Experimental Physics, Moscow, 117259 Russia and*
[3] *INFN, Sezione di Pavia, via Bassi 6, 27100 Pavia , Italy*

Differential cross sections for the process $\gamma n \to \pi^- p$ have been extracted from MAMI-B measurements of $\gamma d \to \pi^- pp$, accounting for final-state interaction effects, using a diagrammatic technique taking into account the NN and πN final-state interaction amplitudes. Results are compared to previous measurements of the inverse process, $\pi^- p \to n\gamma$, and recent multipole analyses.

PACS numbers: 13.60.Le, 24.85.+p, 25.10.+s, 25.20.-x

I. INTRODUCTION

An accurate evaluation of the electromagnetic (EM) couplings $N^*(\Delta^*) \to \gamma N$ from meson photoproduction data remains a paramount task in hadron physics. A wealth of new data for meson photoproduction is becoming available from nuclear facilities worldwide. These measurements are now beginning to have a significant impact on both the resonance spectrum and its decay properties.

Here we focus on the single-pion production data and note that a complete solution requires couplings from both charged and neutral resonances, the latter requiring $\pi^- p$ and $\pi^0 n$ photoproduction off a neutron target, typically a neutron bound in a deuteron target. Extraction of the two-body ($\gamma n \to \pi^- p$ and $\gamma n \to \pi^0 n$) cross sections requires the use of a model-dependent nuclear correction, which mainly come from final state interactions (FSI). As a result, our knowledge of the neutral resonance couplings is less precise as compared to the charged values [1].

In addition to being less precise, experimental data for neutron-target photoreactions are much less abundant than those utilizing a proton target, constituting only about 15% of the present SAID data base [2]. At low to intermediate energies, this lack of neutron-target data is partially compensated by experiments using pionic beams, e.g., $\pi^- p \to \gamma n$, as has been measured, for example, by the Crystal Ball Collaboration at BNL [3] for the inverse photon energy E_γ=285 – 689 MeV and θ=41 – 148°, where θ is the inverse production angle of π^- in the center-of=mass (CM) frame. This process is free from complications associated with the deuteron target. However, the disadvantage of using the reaction $\pi^- p \to \gamma n$ is the 5 to 500 times larger cross sections for $\pi^- p \to \pi^0 n \to \gamma\gamma n$, depending on E_γ and θ.

We recently applied our FSI corrections [4] to CLAS $\gamma d \to \pi^- pp$ data [5] to get elementary cross sections for $\gamma n \to \pi^- p$ [6]. The FSI correction factor for the CLAS kinematics was found to be small, $\Delta\sigma/\sigma$ <10%. However, these new cross sections departed significantly from our predictions, at the higher energies, and greatly modified the fit result.

The present paper is addressed to differential cross section measurements for $\gamma n \to \pi^- p$ in the $\Delta(1232)$-isobar region. At energies dominated by the Delta resonance, the isospin 3/2 multipoles are constrained by extensive studies performed using proton targets. The forward peaking structure is due largely to the Born contribution, which is well known. As a result, one would expect models to give predictions within a tight range, which is confirmed in Figs. 1 and 5.

The paper is organized as follows. In Sec. II, we present the new data set and compare it with previous data from hadronic facilities. Sec. III is devoted to the nuclear corrections. Here, we give comments on the bound neutron and discuss the effect of final state interaction (FSI) corrections. In Sec. IV, we correct the new data for FSI and compare with previous hadronic data and with predictions based on previous multipole analyses. The results of a fit are presented and considered along with the prospect of future polarized measurements.

II. DATA SET

In 2010, the GDH and A2 Collaborations published [7, 8] the first measurement of the unpolarized and the helicity dependent differential cross section for the $\gamma d \to \pi^- pp$ reaction in the Δ-resonance region.

The events from this reaction were selected by requiring the presence of one charged pion and of one or two protons within the detector acceptance (momentum threshold for protons and charged pions ∼270 MeV/c and ∼80 MeV/c, respectively; full azimuthal acceptance and polar laboratory angular acceptance between 21° and 159°)

The obtained results consist of 126 experimental points covering a E_γ range from 301 to 455 MeV and a pion polar angular emission range in the CM system between $\theta = 58^\circ$ and $\theta = 141^\circ$.

During the data analysis phase, a kinematic calculation was performed to evaluate the momentum and the emission angle of the undetected proton. The calculated momentum distribution was found to be almost equal to the Fermi momentum distribution expected from the deuteron wave function (see Fig. 1 of Ref. [7]).

This comparison indicates that the dominant mechanism of the $\gamma d \to \pi^- pp$ channel is the quasi-free reaction on the bound neutron while the proton acts merely as a spectator, remaining approximately at rest in the laboratory system.

MAMI-B deuteron data gives only the differential cross section as function of the pion production laboratory angle and full kinematics was not restored. Thus, the $\gamma n \to \pi^- p$ cross section was extracted assuming the neutron to be at rest to unambiguously relate the pion production angles θ in the $\pi^- p$ CM rest frame to their measured laboratory angles.

Specific examples of agreement with previous measurements are displayed in Fig. 1, where we compare differential cross sections obtained here with those from hadronic facilities (TRIUMF [9], CERN [10], BNL [3], LBL [11], and LAMPF [12]), at energies common to those experiments (within ΔE_γ=5 MeV binning).

III. FSI CALCULATIONS

We extract the $\gamma n \to \pi^- p$ cross section on free nucleon from the deuteron data in the quasi-free (QF) kinematical region of the $\gamma d \to \pi^- pp$ reaction with fast knocked-out proton and slow proton-spectator assumed not to be involved in the pion production process. In this, so-called Impulse-Approximation (IA), the reaction mechanism corresponds to the diagram in Fig. 3(a), and the differential cross section on the deuteron can be related to that on the neutron target in the well-known way (e.g., Eq. (22) of Ref. [4] and references therein). This approximation with additional assumption that the neutron is at rest in the deuteron, allows to identify the cross section $\frac{d\sigma}{d\Omega}$ on the deuteron with that on the neutron, where Ω is the solid angle of the outgoing pion in the γn rest frame. Finally, we use the relation

$$\frac{d\sigma}{d\Omega}(\gamma n) = R^{-1} \frac{d\sigma}{d\Omega}(\gamma d), \qquad (1)$$

where R is the FSI correction factor, which takes into account the FSI effects discussed below as well as the identity of two protons in the γd reaction. The r.h.s. of Eq. (1) contains the cross sections, $\frac{d\sigma}{d\Omega}(\gamma d)$, in the γn rest frame. They were obtained by recalculation of the data [8] on the cross sections, $\frac{d\sigma}{d\Omega}(\gamma d)$, given in the laboratory system (see, Tables I and II), assuming the neutron to be at rest.

There are 2 critical factors to be discussed when using this approach:

1) the neutron is bound and
2) there are NN- and πN-FSI effects.

Item 1) means that effective mass of the neutron

$$m_{eff} = \sqrt{(p_d - p_s)^2} \approx m_n - \epsilon_d - \vec{p}_s{}^2/m_N$$

is not equal to the mass of the free neutron m_n. Here, p_d, p_s, $\vec{p}_s$, ϵ_d, and m_N are the deuteron 4-momentum, 4- and 3-momenta of the spectator, the deuteron binding energy, and the nucleon mass, respectively. Simultaneously, the invariant mass $\sqrt{s_{\pi N}}$ of the final πN-system

$$\sqrt{s_{\pi N}} = \sqrt{s_{\gamma N}} = \sqrt{[(E_\gamma + m_d - E_s)^2 - (\vec{p}_\gamma - \vec{p}_s)^2]}$$

depends on the proton-spectator momentum $\vec{p}_s$ ($s_{\gamma N}$ is the invariant mass squared of the initial γN state). Here, E_γ (E_s), m_d, and $\vec{p}_\gamma$ are the total energy of the initial photon (proton-spectator), the deuteron mass, and the photon 3-momentum, respectively, and $E_\gamma = |\vec{p}_\gamma|$.

Since $\sqrt{s_{\pi N}}$ depends on $\vec{p}_s$, the $\gamma N \to \pi N$ cross section extracted from the deuteron data with undetected nucleon-spectator is averaged over the energy range which depends on kinematical cuts for $\vec{p}_s$. Thus, the "effective" photon lab energy $E_{\gamma n}$, defined through the relation $s_{\gamma N} = m_n^2 + 2m_n E_{\gamma n}$ for the $\gamma n \to \pi^- p$ reaction, is smeared as well as the pion CM angle θ due the deuteron wave function. We estimated this smearing from simplified calculation, where $\gamma d \to \pi^- pp$ amplitude is proportional to the deuteron wave function and depends only on the laboratory momentum of one of the final protons, say p_2, while $E_{\gamma n}$ is determined through the above-mentioned relation with the effective mass of the pion-proton pair with another proton p_1.

Fig. 2 shows distributions on $\Delta E = E_{\gamma n} - E_\gamma$ at $E_\gamma = 301$ and 455 MeV. The distributions peak at $\Delta \approx -3$ MeV, where $E_{\gamma n}$ is very close to E_γ. The dispersion $\sigma(\Delta) = 20.3\,(32.2)$ MeV at $E_\gamma = 301\,(455)$ MeV essentially exceeds the 12-MeV intervals between the plots on Fig. 1. Thus, the neighbour plots on Fig. 1 are quite similar already due to smearing. The plots on Fig. 1 also weakly depend on the energy E_γ in the intervals $\sim \sigma(\Delta)$. Thus, the distortion of the extracted $\gamma n \to \pi^- p$ cross sections due to smearing effect is expected to be small.

The results for the pion CM angle smearing in the angular range of MAMI-B data gives the mean values $\langle\theta\rangle$ very close to θ, namely $|\langle\theta\rangle - \theta| < 1^\circ$, where the pion CM angles θ are obtained from θ_{lab} with the neutron

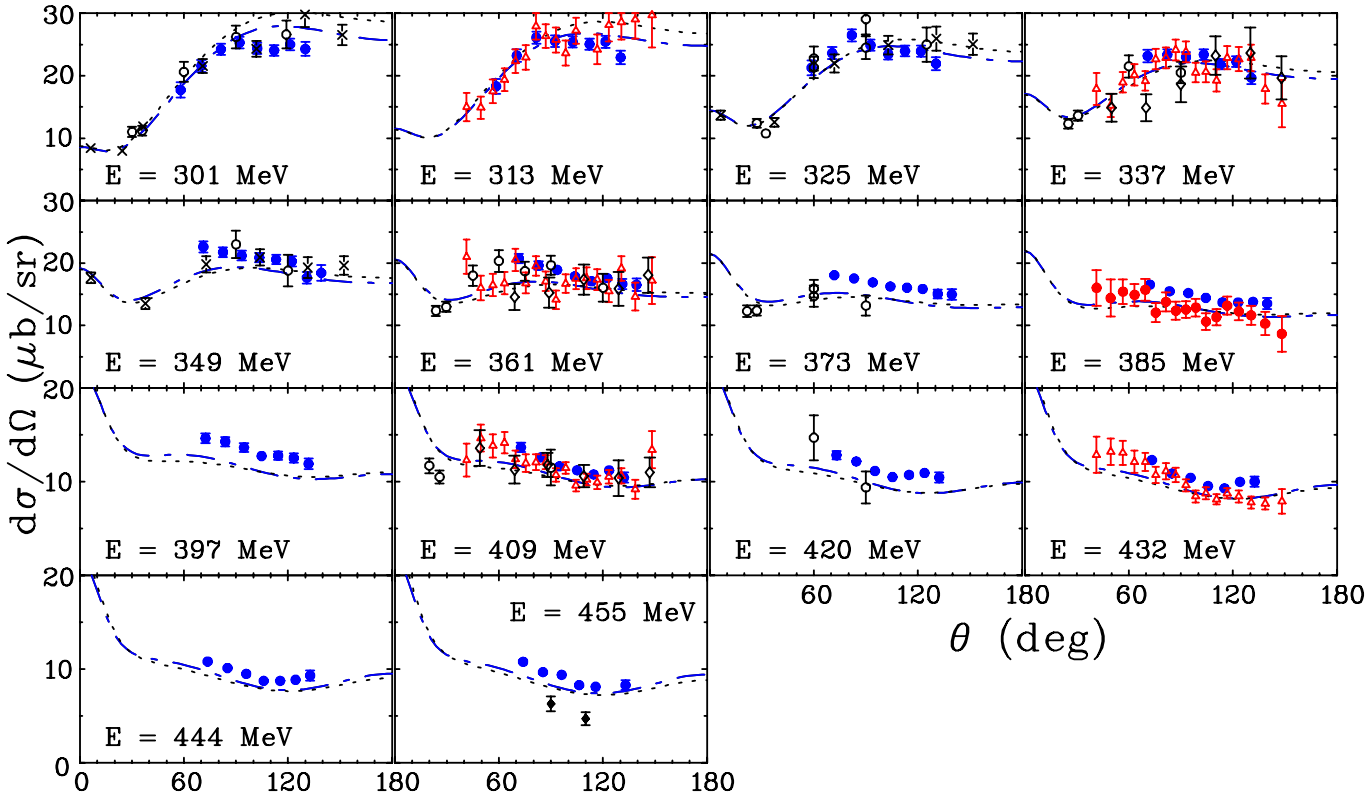

FIG. 1. (Color online) Differential cross sections for $\gamma n \to \pi^- p$ as a function of θ, the production angle of π^- in the CM frame. The present data (solid circles) are shown for 14 energy bins. Previous data came from MAMI-B [7] (blue filled circles), TRIUMF [9] [296, 321, and 346 MeV] (black crosses) CERN [10] [301, 321, 339, 344, 356, 376, 411, and 418] (black open circles), BNL [3] [313, 338, 359, 390, 407, and 436 MeV] (red open triangles), LBL [11] [335, 355, 360, and 409 MeV] (black open dimondes), and LAMPF [12] [458 MeV] (black filled dimonds). Shown data came from hadronic facilities, except MAMI-B measurements (within $\Delta E_\gamma = 5$ MeV binning). Plotted uncertainties are statistical only. Blue dash-dotted (black dotted) lines correspond to the predictions for our recent SN11 [13] (MAID07 [14]) solution.

at rest. The angle dispersion $\sigma(\theta)$ varies in the interval $\sim (3.0 - 5.5)^\circ$.

Item 2) corresponds to the inclusion of the FSI corrections. Their leading terms correspond to Feynman diagrams shown on Fig. 3(b,c).

Calculations of the $\gamma d \to \pi^- pp$ differential cross sections, with the FSI taken into account (all the diagrams on Fig. 3, were included) were done as we did recently [4, 6] for the CLAS data ($E_\gamma = 1050 - 2700\ MeV$ and $\theta = 32 - 157^\circ$) [5]. The SAID phenomenological amplitudes for $\gamma N \to \pi N$ [15], NN-elastic [16], and πN-elastic [17] were used as inputs to calculate the diagrams in Fig. 3. The Bonn potential [18] was used for the deuteron description. In Ref. [6], we calculated the FSI correction factor R dependent on E_γ and θ (see details in Refs. [4, 6]), and fitted these CLAS data vs. the world $\gamma N \to \pi N$ database [2] to get new multipoles and determine resonance EM couplings [6]. The FSI corrections for the CLAS "quasi-free" kinematics were found to be small, as mentioned above. Our FSI calculations were done [4] over the broad energy range (threshold to 2700 MeV for E_γ) and for the full angular coverage ($\theta = 0 - 180^\circ$). As an illustration, Fig. 4 shows the FSI correction factor $R = R(E_\gamma, \theta)$ for the present $\gamma n \to \pi^- p$ differential cross sections as a function of the pion production angle in the CM($\pi^- p$) frame, θ, for different energies over the range of the MAMI-B experiment. Overall, the FSI correction factor $R < 1$, while the effect, i.e., the $(1 - R)$ value varied from 10% to 30% depending on the kinematics and the behavior is very smooth vs. pion production angle. Note that $R(E_\gamma, \theta)$ is the FSI correction factor for the $\gamma n \to \pi^- p$ cross section averaged over the lab photon energy $E_{\gamma n}$. Fig. 3 shows that R depends slowly on the energy in the intervals $\sim \sigma(\Delta)$. Thus, smearing effect illustrated on Fig. 2, weakly affects the FSI correction procedure for the extracted $\gamma n \to \pi^- p$ cross section at a given energies.

The contribution of FSI calculations [4] to the overall

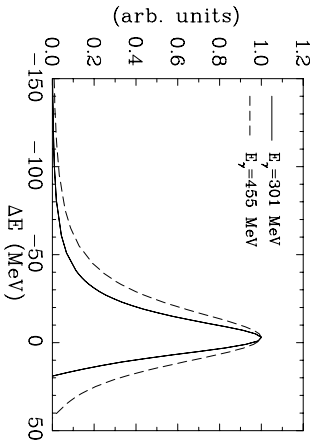

FIG. 2. Distributions on the shift $\Delta E = E_{\gamma n} - E_\gamma$ of the effective photon laboratory energy $E_{\gamma n}$ on the neutron target at $E_\gamma = 301$ MeV (solid curve) and 455 MeV (dashed curve). The mean values are $\sigma(\Delta) = -12\,(-14.6)$ MeV for $E_\gamma = 301\,(455)$ MeV.

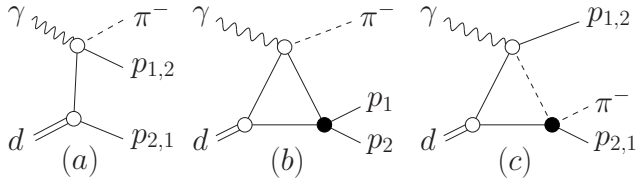

FIG. 3. Feynman diagrams for the leading terms of the $\gamma d \to \pi^- pp$ amplitude. (a) IA, (b) pp-FSI, and (c) πN-FSI. Filled black circles show FSI vertices. Wavy, dashed, solid, and double lines correspond to the photons, pions, nucleons, and deuterons, respectively.

systematics is estimated to be 2%.

IV. RESULTS

In fitting the database, χ^2 is calculated using

$$\chi^2 = \sum_i^{N_{data}} \left(\frac{O_i - N_j O_i^{exp}}{\delta O_i} \right)^2 + \sum_j^{N_{dist}} \left(\frac{N_j - 1}{\delta N_j} \right)^2, \quad (2)$$

where O_i and O_i^{exp} are calculated and experimental observables, for a given energy and angle, and δO_i is the statistical uncertainty. The systematic error, δN_j, for a given angular distribution, is used to calculate a second contribution to χ^2 due to overall normalization (N_j) of angular datasets.

In Fig. 1, which compares the present measurements with corresponding results derived from pion-induced reactions, no FSI (nor any data renormalization) corrections have been applied. The curves are predictions from SAID and MAID and are generally quite consistent. Without corrections, the pion- and photo-induced data are reasonably consistent where they can be compared (the pion-induced results having significantly larger uncertainties). Comparisons with the SAID and MAID predictions show reasonable agreement in terms of shape but, at a number of energies, there is a clear difference in the overall normalization.

In Fig. 5, both FSI and data renormalization have been applied. A solid curve, giving the result of a fit, is compared with the aforementioned predictions. The data renormalization, required for a best-fit result, changes from an average of 7%, for the SAID prediction, to about 4.5%,after the data have been included in the fit. In both cases, the second term in Eq. (2) above (due to renormalization) contributes nearly 50% to the total chi-squared.

Changes to the multipoles in the revised fit are small. The dominant multipole contribution from the $\Delta(1232)$ is not changed significantly, as one would expect. Together with the measurements of Ref. [6], we now have a nearly complete coverage of the resonance region for unpolarized cross sections, in this reaction. Further progress will require polarized measurements, which are expected from the CLAS Collaboration [19].

The MAMI-B results for the $\gamma d \to \pi^- pp$ differential cross sections in laboratory frame, $\frac{d\sigma}{d\Omega}(\gamma d)$, consist of 126 experimental points ($E_\gamma = 301 - 455\ MeV$ and $\theta_{lab} = 45 - 125^\circ$), they are tabulated in Ref. [8]. For the reader convenience these data with the final $\gamma n \to \pi^- p$ ones in CM frame, $\frac{d\sigma}{d\Omega}(\gamma n)$, are also shown in Tables I and II along with their uncertainties.

The χ^2 contribution of MAMI-B data (including FSI corrections) is $\chi^2/\text{data} = 249.4/104 = 2.4$ while, prior to fitting, for SN11 [13] (MAID07 [14]), we had $\chi^2/\text{data} = 605.8/104 = 5.8$ ($623.2/104 = 6.0$).

The MAMI-B data (including FSI corrections) and the results from hadronic data appear to agree well at these energies (Fig. 4). In particular, the χ^2 contribution from recent CB@BNL [3] and MAMI-B measurements at 6 overlapped energies [313, 337, 361, 385, 409, and 432 MeV] results $\chi^2/\text{data} = 97.7/102 = 1.0$ and $\chi^2/\text{data} = 103.9/45 = 2.3$, respectively, for the PE12 solution. While for previous SN11 solution [13], it gives $\chi^2/\text{data} = 87.4/102 = 0.9$ and $\chi^2/\text{data} = 188.6/45 = 4.2$, respectively (MAMI-B data had no FSI corrections).

V. SUMMARY AND CONCLUSION

A comprehensive set of differential cross sections at 14 energies for negative-pion photoproduction on the neutron, via the reaction $\gamma d \to \pi^- pp$, have been determined with a MAMI-B tagged-photon beam for incident photon

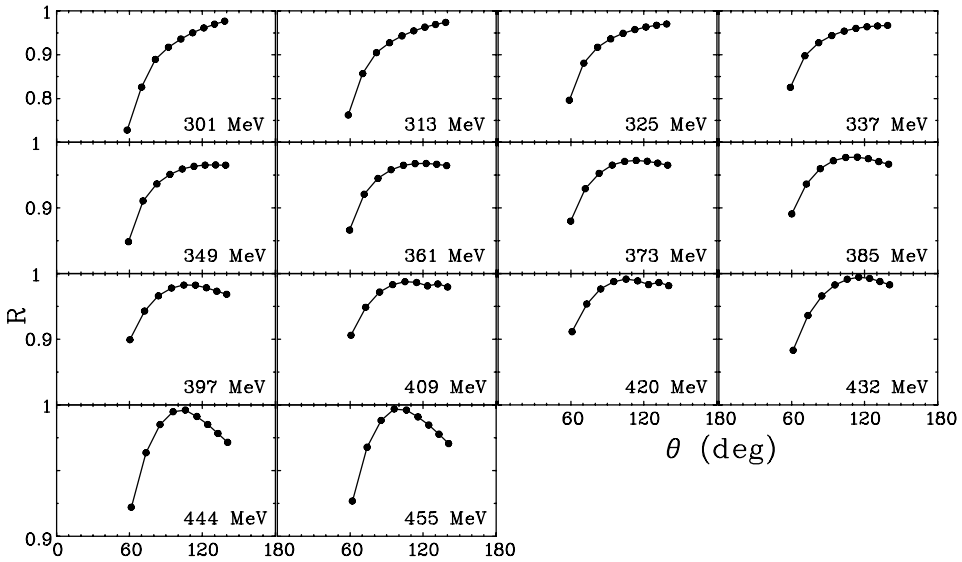

FIG. 4. FSI correction factor R for $\gamma n \to \pi^- p$ as a function of θ, where θ is the production angle of π^- in the CM frame. The present calculations (solid circles) are shown for 14 energy bins. There are no uncertaintes given. Curves may help to lead eyes.

energies from 301 to 455 MeV. To accomplish a state-of-the-art analysis, we included FSI corrections using a diagrammatic technique, taking into account a kinematical cut with momenta less (more) than $\sim$270 MeV/c for slow (fast) outgoing protons.

On the experimental side, further improvements in the PWAs await more data, specifically in the region above 1 GeV, where the number of measurements for this reaction is small. Of particular importance in all energy regions is the need for data obtained involving polarized photons and/or polarized targets. Some of these data are already available in Ref. [6]. Due to the closing of hadron facilities, new $\pi^- p \to \gamma n$ experiments are not planned and only $\gamma n \to \pi^- p$ measurements are possible at electromagnetic facilities using deuterium targets. Our agreement with existing π^- photoproduction measurements leads us to believe that these photoproduction measurements are reliable despite the necessity of using a deuterium target.

Obviously, any meson photoproduction treatment on the "neutron" target requires a FSI study. Generally, FSI depends on the full set of kinematical variables of the reaction. In our analysis, the FSI correction factor depends on the photon energy, meson production angle, and is averaged on the rest of variables in the region of "quasi-free" process on the neutron.

ACKNOWLEDGMENTS

We acknowledge the outstanding efforts of the GDH and A2 Collaborations who made the experiment possible. This work was supported in part by the U.S. Department of Energy Grant No. DE–FG02–99ER41110, by the Russian RFBR Grant No. 02–0216465, by the Russian Atomic Energy Corporation "Rosatom" Grant No. NSb–4172.2010.2, and the Italian Istituto Nazionale di Fisica Nucleare.

TABLE I. Differential cross sections for $\gamma d \to \pi^- pp$ [8] (statistical and systematical uncertainties are given separately which we then combined in quadratures) and final $\gamma n \to \pi^- p$ below 400 MeV. Differential cross section, $\frac{d\sigma}{d\Omega}(\gamma d)$, is given in lab frame while $\frac{d\sigma}{d\Omega}(\gamma n)$ is given in CM frame.

Energy (MeV)	θ_{lab} (deg)	$\frac{d\sigma}{d\Omega}(\gamma d)$ (μb/sr)	θ (deg)	$\frac{d\sigma}{d\Omega}(\gamma n)$ (μb/sr)	Energy (MeV)	θ_{lab} (deg)	$\frac{d\sigma}{d\Omega}(\gamma d)$ (μb/sr)	θ (deg)	$\frac{d\sigma}{d\Omega}(\gamma n)$ (μb/sr)
301.0	45.0	18.73±1.09±0.68	58.1	17.71±1.22	313.0	45.0	20.38±1.08±0.74	58.4	18.30±1.18
	55.0	23.70±0.74±0.76	70.0	21.59±0.97		55.0	26.54±0.71±0.85	70.3	23.22±0.97
	65.0	25.96±0.54±0.83	81.3	24.23±0.93		65.0	28.49±0.53±0.91	81.6	26.11±0.97
	75.0	25.20±0.43±0.81	92.1	25.30±0.92		75.0	25.68±0.42±0.82	92.3	25.52±0.92
	85.0	22.28±0.38±0.69	102.3	24.37±0.86		85.0	23.33±0.39±0.72	102.6	25.39±0.89
	95.0	20.11±0.38±0.62	112.0	24.06±0.87		95.0	20.95±0.38±0.65	112.3	25.05±0.90
	105.0	19.13±0.42±0.59	121.2	25.02±0.95		105.0	19.38±0.42±0.60	121.4	25.44±0.96
	115.0	17.05±0.47±0.62	130.0	24.28±1.11		115.0	15.98±0.47±0.58	130.2	22.92±1.07
	125.0	14.47±0.59±0.53	138.3	22.28±1.22		125.0	14.36±0.63±0.52	138.5	22.34±1.27
325.0	45.0	24.88±1.04±0.91	58.7	21.27±1.18	337.0	45.0	26.35±1.28±0.96	58.9	21.60±1.31
	55.0	27.84±0.66±0.89	70.5	23.62±0.94		55.0	27.93±0.80±0.89	70.9	23.17±1.00
	65.0	29.33±0.50±0.94	81.9	26.48±0.96		65.0	26.23±0.46±0.84	82.2	23.39±0.85
	75.0	25.25±0.41±0.81	92.7	24.88±0.89		75.0	23.49±0.39±0.75	93.0	22.97±0.83
	85.0	21.60±0.37±0.67	102.9	23.42±0.83		85.0	21.62±0.38±0.67	103.2	23.38±0.83
	95.0	20.00±0.38±0.62	112.5	23.95±0.87		95.0	18.20±0.37±0.56	112.8	21.83±0.81
	105.0	18.13±0.41±0.56	121.7	23.93±0.92		105.0	16.78±0.41±0.52	122.0	22.27±0.88
	115.0	15.15±0.47±0.55	130.4	21.92±1.05		115.0	13.47±0.46±0.49	130.6	19.66±0.98
	125.0	13.36±0.63±0.49	138.7	21.03±1.25		125.0	12.31±0.64±0.45	138.9	19.59±1.24
349.0	45.0	26.48±0.90±0.96	59.2	20.99±1.05	361.0	45.0	26.32±0.68±0.96	59.5	20.32±0.91
	55.0	27.74±0.59±0.89	71.2	22.60±0.87		55.0	25.83±0.44±0.83	71.5	20.74±0.75
	65.0	24.64±0.44±0.79	82.5	21.73±0.80		65.0	22.48±0.34±0.72	82.8	19.62±0.70
	75.0	21.82±0.38±0.70	93.3	21.19±0.77		75.0	19.59±0.29±0.63	93.6	18.90±0.67
	85.0	19.34±0.36±0.60	103.5	20.86±0.75		85.0	16.63±0.27±0.51	103.8	17.89±0.62
	95.0	17.14±0.36±0.53	113.1	20.58±0.77		95.0	14.22±0.27±0.44	113.4	17.08±0.62
	105.0	15.22±0.39±0.47	122.2	20.29±0.81		105.0	13.15±0.30±0.41	122.5	17.59±0.68
	115.0	12.00±0.45±0.44	130.9	17.65±0.92		115.0	11.25±0.36±0.41	131.1	16.66±0.81
	125.0	11.46±0.65±0.42	139.1	18.43±1.24		125.0	10.18±0.51±0.37	139.3	16.52±1.02
373.0	45.0	24.47±0.50±0.89	59.8	18.50±0.77	385.0	45.0	23.06±0.49±0.84	60.1	17.12±0.72
	55.0	22.77±0.32±0.73	71.8	18.05±0.63		55.0	21.11±0.30±0.68	72.1	16.55±0.58
	65.0	20.29±0.26±0.65	83.2	17.54±0.61		65.0	18.05±0.24±0.58	83.5	15.47±0.54
	75.0	17.64±0.23±0.57	93.9	16.91±0.59		75.0	15.94±0.22±0.51	94.3	15.19±0.53
	85.0	15.16±0.21±0.47	104.1	16.25±0.55		85.0	13.50±0.21±0.42	104.4	14.43±0.50
	95.0	13.37±0.22±0.41	113.7	16.05±0.56		95.0	11.42±0.20±0.35	114.0	13.71±0.49
	105.0	11.82±0.24±0.36	122.8	15.85±0.59		105.0	10.18±0.22±0.31	123.0	13.69±0.52
	115.0	10.12±0.29±0.37	131.4	15.07±0.70		115.0	9.22±0.28±0.34	131.6	13.80±0.65
	125.0	9.16±0.40±0.33	139.5	14.98±0.85		125.0	8.21±0.44±0.30	139.7	13.52±0.88
397.0	45.0	22.55±0.42±0.82	60.4	16.49±0.67	397.0	55.0	18.85±0.28±0.60	72.4	14.63±0.52
	65.0	16.79±0.24±0.54	83.8	14.28±0.50		75.0	14.39±0.21±0.46	94.6	13.64±0.48
	85.0	11.95±0.20±0.37	104.7	12.74±0.45		95.0	10.65±0.20±0.33	114.3	12.78±0.46
	105.0	9.29±0.22±0.29	123.3	12.53±0.49		115.0	7.92±0.27±0.29	131.8	11.91±0.59
	125.0	7.84±0.42±0.29	139.9	13.00±0.84					

TABLE II. Differential cross sections for $\gamma d \to \pi^- pp$ [8] (statistical and systematical uncertainties are given separately which we then combined in quadratures) and final $\gamma n \to \pi^- p$ above 400 MeV. Differential cross section, $\frac{d\sigma}{d\Omega}(\gamma d)$, is given in lab frame while $\frac{d\sigma}{d\Omega}(\gamma n)$ is given in CM frame.

Energy (MeV)	θ_{lab} (deg)	$\frac{d\sigma}{d\Omega}(\gamma d)$ (μb/sr)	θ (deg)	$\frac{d\sigma}{d\Omega}(\gamma n)$ (μb/sr)	Energy (MeV)	θ_{lab} (deg)	$\frac{d\sigma}{d\Omega}(\gamma d)$ (μb/sr)	θ (deg)	$\frac{d\sigma}{d\Omega}(\gamma n)$ (μb/sr)
409.0	45.0	21.34±0.44±0.78	60.6	15.40±0.64	420.0	45.0	20.43±0.37±0.74	60.9	14.58±0.59
	55.0	17.77±0.27±0.57	72.7	13.66±0.48		55.0	16.83±0.27±0.54	73.0	12.83±0.46
	65.0	14.92±0.23±0.48	84.2	12.60±0.45		65.0	14.48±0.23±0.46	84.5	12.16±0.44
	75.0	12.32±0.20±0.39	94.9	11.63±0.42		75.0	11.84±0.20±0.38	95.2	11.14±0.40
	85.0	10.55±0.19±0.33	105.1	11.22±0.40		85.0	9.88±0.19±0.31	105.3	10.50±0.38
	95.0	8.97±0.19±0.28	114.6	10.77±0.40		95.0	8.91±0.19±0.28	114.9	10.72±0.40
	105.0	8.28±0.21±0.26	123.6	11.20±0.45		105.0	8.05±0.22±0.25	123.8	10.93±0.45
	115.0	6.96±0.26±0.25	132.1	10.43±0.54		115.0	6.94±0.27±0.25	132.3	10.45±0.56
	125.0	7.72±0.48±0.28	140.2	12.77±0.92		125.0	6.92±0.48±0.25	140.3	11.51±0.90
432.0	45.0	19.41±0.39±0.71	61.2	14.22±0.59	444.0	45.0	17.83±0.37±0.65	61.5	12.44±0.52
	55.0	15.89±0.26±0.51	73.3	12.30±0.44		55.0	14.41±0.25±0.46	73.6	10.80±0.39
	65.0	12.81±0.22±0.41	84.8	10.87±0.40		65.0	12.16±0.22±0.39	85.1	10.12±0.37
	75.0	11.00±0.20±0.35	95.6	10.41±0.38		75.0	10.14±0.19±0.33	95.9	9.49±0.35
	85.0	8.94±0.19±0.28	105.7	9.53±0.36		85.0	8.21±0.18±0.25	106.0	8.74±0.33
	95.0	7.73±0.19±0.24	115.2	9.29±0.37		95.0	7.21±0.18±0.22	115.4	8.74±0.35
	105.0	7.37±0.22±0.23	124.1	9.98±0.43		105.0	6.45±0.21±0.20	124.4	8.86±0.40
	115.0	6.61±0.28±0.24	132.5	10.01±0.56		115.0	6.04±0.27±0.22	132.8	9.31±0.54
	125.0	7.25±0.51±0.26	140.5	12.15±0.96		125.0	6.24±0.50±0.23	140.8	10.68±0.94
455.0	45.0	17.45±0.37±0.64	61.7	12.05±0.51	455.0	55.0	14.48±0.26±0.46	73.9	10.78±0.40
	65.0	11.68±0.22±0.37	85.4	9.67±0.36		75.0	10.03±0.20±0.32	96.2	9.38±0.35
	85.0	7.76±0.18±0.24	106.3	8.28±0.32		95.0	6.66±0.18±0.21	115.7	8.11±0.33
	105.0	7.00±0.22±0.22	124.6	9.67±0.43		115.0	5.33±0.28±0.19	133.0	8.28±0.53
	125.0	5.46±0.51±0.20	140.9	9.42±0.95					

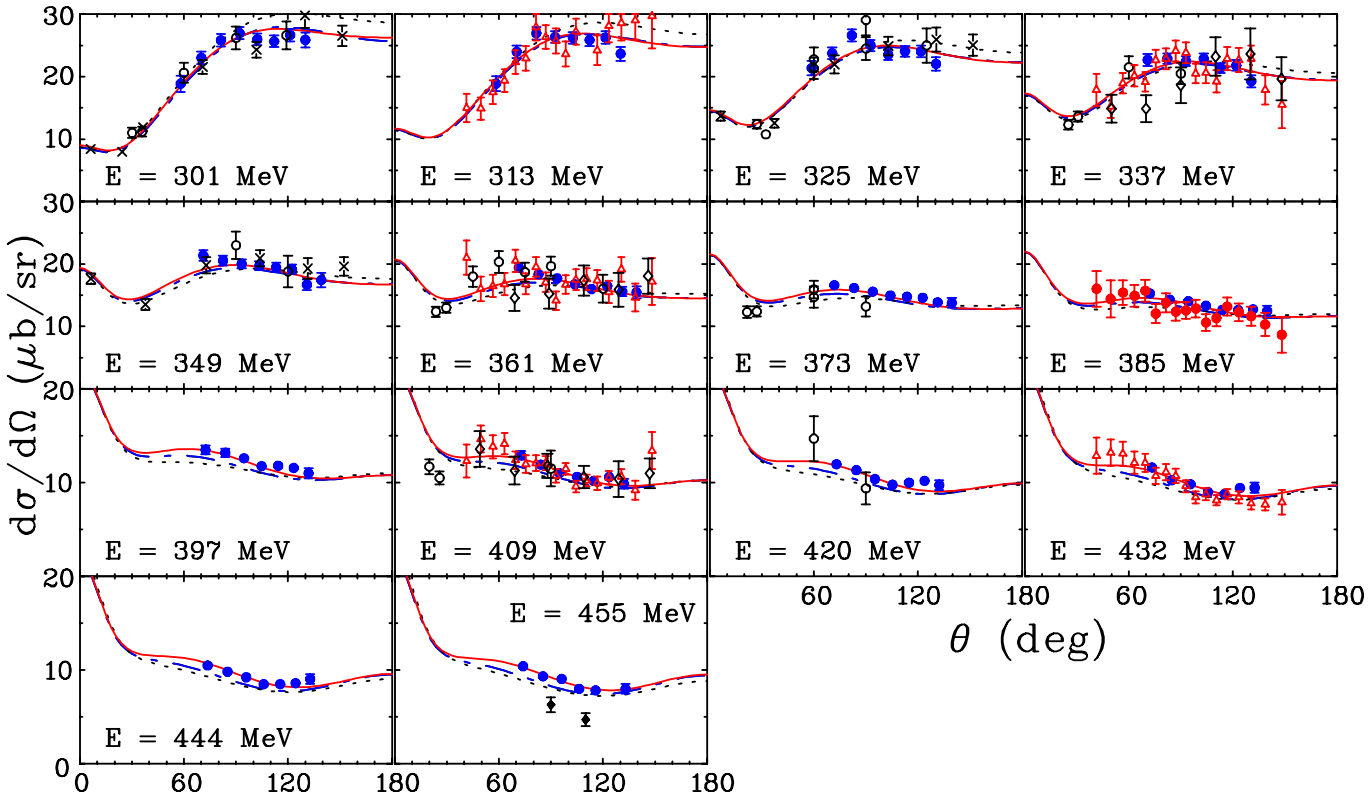

FIG. 5. (Color online) Differential cross sections for $\gamma n \to \pi^- p$ as a function of θ, where θ is the production angle of π^- in the CM frame. Notation of data and solutions are the same as in Fig. 1. MAMI-B data including in the PE12 fit (red solid line).

[1] J. Beringer *et al.* (Particle Data Group), Phys. Rev. D **86**, 010001 (2012).

[2] W. J. Briscoe, I. I. Strakovsky, and R. L. Workman, Institute of Nuclear Studies of The George Washington University Database; http://gwdac.phys.gwu.edu/analysis/pr_analysis.html .

[3] A. Shafi, *et al.* (Crystal Ball Collaboration), Phys. Rev. C **70**, 035204 (2004).

[4] V. E. Tarasov *et al.*, Phys. Ref. C **84**, (2011) 035203.

[5] W. Chen, *el al.* (CLAS Collaboration), Phys. Rev. Lett. **103**, 012301 (2009).

[6] W. Chen, *el al.* Phys. Rev. C **86**, 015206 (2012).

[7] J. Ahrens, *et al.* (GDH and A2 Collaborations), Eur. Phys. J. A **44**, 189 (2010).

[8] M. M. Fabregate, Ph. D. Thesis, Mainz Univ. 2007.

[9] M. Wang, Ph. D. Thesis, University of Kentucky, 1992.

[10] M. T. Tran, *et al.*, Nucl. Phys. **A324**, 301 (1979).

[11] J. C. Comiso, *et al.*, Phys. Rev. D **12**, 719 (1975).

[12] G. J. Kim, *et al.*, Phys. Rev. D **40**, 244 (1989).

[13] R. L. Workman, W. J. Briscoe, M. W. Paris, and I. I. Strakovsky, Phys. Rev. C **85**, 025201 (2012).

[14] D. Drechsel, S. S. Kamalov, and L. Tiator, Eur. Phys. J. A **34**, 69 (2007); http://www.kph.uni-mainz.de/MAID/.

[15] M. Dugger, *et al.* (CLAS Collaboration), Phys. Rev. C **76**, 025211 (2007).

[16] R. A. Arndt, *et al.*, Phys. Rev. C **76**, (2007) 025211.

[17] R. A. Arndt, *et al.*, Phys. Rev. C **74**, (2006) 045205.

[18] R. Machleidt, *et al.*, Phys. Rept. **140**, (1987) 1.

[19] D. Sokhan, Ph. D. Thesis, Edinburgh University, 2009.